Cooling rate dependence of structural order in $Al_{90}Sm_{10}$ metallic glass

Yang Sun[1,2], Yue Zhang[2], Feng Zhang[2]*, Zhuo Ye[2], Zejun Ding[1], Cai-Zhuang Wang[2,3], Kai-Ming Ho[1,2,3]

[1]Hefei National Laboratory for Physical Sciences at the Microscale and Department of Physics, University of Science and Technology of China, Hefei, Anhui 230026, China

[2]Ames Laboratory, US Department of Energy, Ames, Iowa 50011, USA

[3]Department of Physics, Iowa State University, Ames, Iowa 50011, USA

Abstract

The atomic structure of $Al_{90}Sm_{10}$ metallic glass is studied using molecular dynamics simulations. By performing a long sub-T_g annealing, we developed a glass model closer to the experiments than the models prepared by continuous cooling. Using the cluster alignment method, we found "3661" cluster is the dominating short-range order in the glass samples. The connection and arrangement of "3661" clusters, which define the medium-range order in the system, are enhanced significantly in the sub-T_g annealed sample as compared to the fast cooled glass samples. Unlike some strong binary glass formers such as $Cu_{64.5}Zr_{35.5}$, The clusters representing the short-range order do not form an interconnected interpenetrating network in $Al_{90}Sm_{10,}$ which has only marginal glass formability.

*To whom correspondence may be addressed: fzhang@ameslab.gov

Introduction

Since the first metallic glass (MG) is discovered in 1960s [1], there has been extensive interest in developing and understanding this new family of materials [2–8]. Among many unresolved puzzles, a fundamental issue is to understand the underlying structural order in MGs [9]. Although MGs do not have well-defined long-range order as crystalline metals, many recent experiments [10–12] and theoretical modeling [13–20] have reported short- to medium-range order in MG systems. Here, the short-range order (SRO) is commonly defined as the local atomic arrangement within the first coordination shell, while the medium-range order (MRO) refers to the next-level structural organization such as the spatial correlations of the local structural 'units' which are connected and arranged to fill three-dimensional space[17].

Aluminum-rare-earth (Al-RE) alloys have been well demonstrated to form glasses under rapid quenching from liquid melts. The as-formed glasses, usually containing more than 85 at.% Al, have much desired large strength-to-weight ratio. The Al-Sm system is a representative member of the Al-RE alloys and offers the widest glass forming composition range in the Al-RE series [21]. Furthermore, an array of stable and metastable crystalline phases are also attainable from the glass phase upon reheating [22–25]. Our previous studies have revealed a dominating SRO represented by a Sm-centered "3661" motif as shown in Fig. 1, in which the first-shell atoms form a top triangle, two consecutive hexagons, and a bottom atom, in the $Al_{90}Sm_{10}$ undercooled liquid[26]. It should be noted that the "3661" motif is representative of a series of similar clusters[26]. Interestingly, the same packing motif was also found in two metastable crystalline phases in devitrified $Al_{90}Sm_{10}$ MG [27,28]. In order to understand the amorphization and

devitrification processes of $Al_{90}Sm_{10}$, a critical question to ask is how the "3661"-type SRO evolves and extends to medium-range order (MRO) upon glass transition.

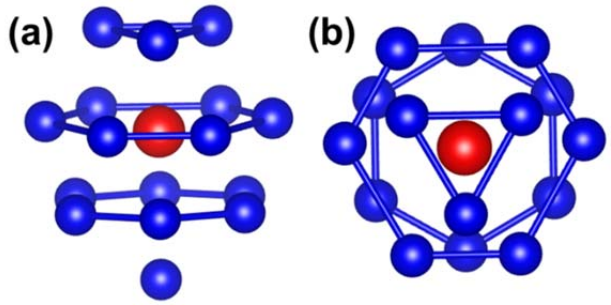

FIG. 1 (a) The side view of "3661" motif; (b) the top view of "3661" motif. The red atom indicates the center Sm, while the blue atoms indicate the first-shell atoms.

As molecular dynamics (MD) simulations can provide detailed atomic trajectories, it has become a powerful tool for investigating the structures and properties of MGs [29]. To generate MG samples, rapid cooling from metallic liquids is widely used in both experiments and computer simulations [30–32]. Such rapid cooling forbids the formation of crystalline phase and drives system to glassy state under the far-from-equilibrium condition. In such rapid solidification processes, the phase selection is critically dependent on the cooling rate[30]. It would be desirable to use the same cooling rate in computer simulation as that in the real experiment in order to have a fair comparison between the simulation results and experimental measurements. However, time scale is a big challenge in most of the current atomistic simulations and a large gap of cooling rate between the simulated MG (faster than 10^9 K/s) and real MG from experiments (~10^3-10^6 K/s) [31] is commonly found in the literature. Recently, it has been demonstrated that annealing simulated samples below but close to the glass transition temperature (sub-T_g) can effectively accelerate structural relaxation and help achieve a more realistic atomistic model for MG [33,34]. In this paper, we employ the sub-T_g annealing method to investigate

the evolution of the structural order of $Al_{90}Sm_{10}$ MG by MD simulations. MG samples have been generated with an effective cooling rate as slow as 5.7×10^7 K/s, which is about two orders of magnitude lower than conventional cooling rates used in most of the MD simulations. Based on the partial pair correlation functions (PCF), we show that the Sm-Sm pair correlation in the sub-T_g annealed samples changes dramatically from fast cooled samples. This change results in a structure factor much closer to experiments. Using the cluster alignment method [35], "3661" SRO surrounding Sm atoms is found to be abundant in the glass samples. Comparing the samples with different cooling process, we show a significant impact of lowering effective cooling rates on the enhancement of SRO and MRO in the MG models.

Methods

To perform long-time, large scale MD simulation, we employ a semi-empirical potential[36] in the Finnis-Sinclair form for the energy calculations. This potential has been demonstrated to well reproduce the pair distribution functions of $Al_{90}Sm_{10}$ liquid in equilibrium (above the melting point) from *ab initio* MD simulations[36]. In Fig. 2, we show the pair distribution functions, as well as the distribution of the alignment score with the "3661" motif, obtained by both classical and *ab initio* MD simulations for *undercooled* $Al_{90}Sm_{10}$ liquid at 800 K, which again show favorable comparisons. The constant number of atoms, pressure, and temperature (NPT) ensemble is applied with Nose-Hoover thermostats. The time step of the simulation is 2.5 *fs*. The liquid sample, containing 4500 Al atoms and 500 Sm atoms, are initially held at 2000K for 2.5 ns to reach equilibrium. Then the liquid is continuous cooled down with a constant rate 10^{10} K/s to 650K, which is below the $T_g \sim 693$K [36]. After that, the as-quenched sample is

annealed isothermally at 650 K for 843 ns, followed by a continuous cooling at 10^{10} K/s to 300K. The total simulation time spent on the process was 1013 ns, corresponding to an averaged cooling rate 1.68×10^{9} K/s. To demonstrate the effect of the sub-T_g annealing, five other $Al_{90}Sm_{10}$ glass samples are generated using uniform continuous cooling from 2000K to 300K with different cooling rate at 10^{13}, 10^{12}, 10^{11}, 10^{10} and 10^{9} K/s, respectively. In order to eliminate the effect of atomic thermal motions on local atomic structures, the averaged atomic positions over 10000 successive MD steps at 300 K are used to represent the structure of each glass sample.

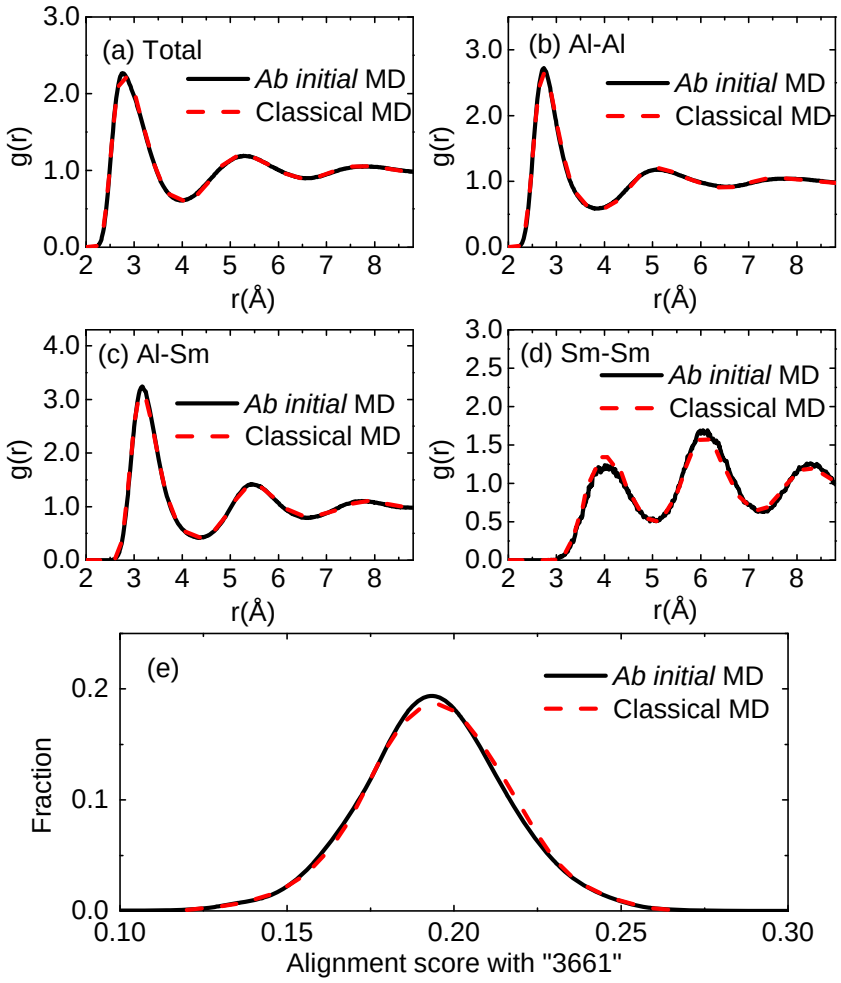

FIG. 2 The validation of AlSm Finnis-Sinclair potential. (a)-(d) The comparison of total and partial pair distribution functions of $Al_{90}Sm_{10}$ undercooled liquid at 800 K obtained

by previous *ab initial* MD[26] and current classical MD with the Finnis-Sinclair potential. (e) The comparison of alignment score with "3661" template for Sm atoms in $Al_{90}Sm_{10}$ liquid at 800 K obtained by *ab initial* MD and classical MD.

The total structure factors $S(q)$ of the MD samples are calculated with the Faber-Ziman formalism [37]:

$$S(q) = \varpi_{11}S_{11}(q) + \varpi_{12}S_{12}(q) + \varpi_{22}S_{22}(q), \quad (1)$$

where the subscripts 1 and 2 refer to Al and Sm species, respectively. The weight factor ϖ_{ij} are determined by the composition (molar fraction) of the two species c_1 and c_2 and the q-dependent atomic scattering factors $f_1(q)$ and $f_2(q)$ [38]:

$$\begin{cases} \varpi_{11} = \frac{c_1^2 f_1^2(q)}{[c_1 f_1(q)+c_2 f_2(q)]^2}, \\ \varpi_{12} = \frac{2c_1 c_2 f_1(q) f_2(q)}{[c_1 f_1(q)+c_2 f_2(q)]^2}, \\ \varpi_{22} = \frac{c_2^2 f_2^2(q)}{[c_1 f_1(q)+c_2 f_2(q)]^2}. \end{cases} \quad (2)$$

$S_{ij}(q)$ in Eq. (1) are the partial structure factors which can be obtained by Fourier transform of the corresponding partial pair correlation functions:

$$S_{ij}(q) = 1 + 4\pi\rho \int_0^\infty \left[g_{ij}(r) - 1\right] \frac{\sin(qr)}{r} r dr \ , \quad (3)$$

where ρ is the number density of the relevant atom species in the sample.

The SRO is analyzed by checking the similarity of local clusters extracted from MD samples to certain template motifs, using the cluster alignment method. An alignment score, describing how the aligned cluster deviates from the motif, is defined as

$$f = \min_{0.80 \le \alpha \le 1.2} \left(\frac{1}{N} \sum_{i=1}^{N} \frac{(\vec{r}_{ic} - \alpha \vec{r}_{it})^2}{(\alpha \vec{r}_{it})^2} \right)^{1/2} \quad (4),$$

where N is the number of the neighbor atoms in the template; $\vec{r}_{ic}$ and $\vec{r}_{it}$ are the atom positions in the aligned cluster and template, respectively; and α is a coefficient to adapt

the template's bond length. The range of α is between 0.8 and 1.2, which allows a large enough "breathing" room for the bond length in templates, in order to achieve an optimal alignment. The smaller score indicates a higher similarity between the cluster and the template.

Results and discussions

In order to show the effectiveness of sub-T_g annealing on this system, we first show the potential energy, which is an important parameter to measure the stability of the glass samples[39], in Fig. 3 at $T = 300$ K for all the models with different cooling processes. One can see a linear dependence of the potential energy on the logarithm of the cooling rate for the continuously cooled samples. Such behavior is also observed in the Cu-Zr system [33,34]. Assuming the linear relationship persists for even lower cooling rates, extrapolation of the least-square fitting yields an effective continuous cooling rate of 5.7 × 10^7 K/s for the sample annealed at 650 K. Therefore, this sub-T_g annealing approach speeds up the simulation by 28 times in comparison with the simulation under uniform continuous cooling using the same computer time.

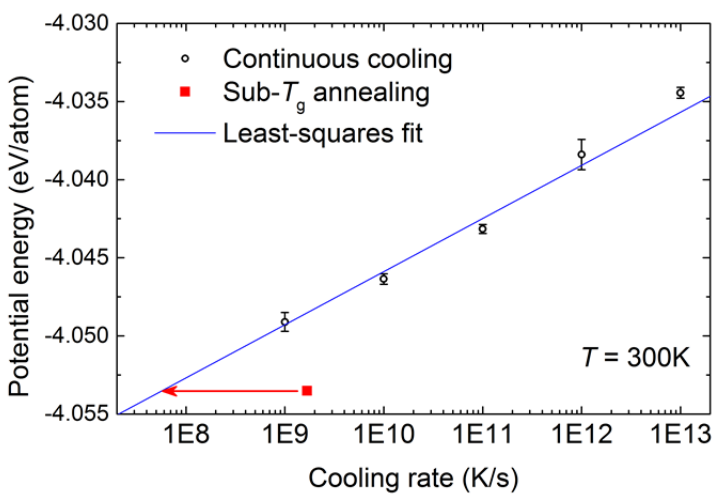

FIG. 3 Potential energy at 300K as a function of cooling rate. The blue line is the least-square fitting to a logarithmic dependence for all continuous cooled samples. The red

arrow points an effective continuous cooling rate of 5.7×10^7 K/s achieved by sub-T_g annealing.

The sub-T_g annealing of $Al_{90}Sm_{10}$ glass provides a more realistic glass model to investigate how the structural order evolves in the glassy state during the simulations. In Fig. 4 (a)-(c), we plot the partial pair correlation functions $g(r)$ for all the simulated samples, which clearly exhibits amorphous features as characterized by attenuating broad peaks. In Fig. 4(a), although the peaks of $g_{AlAl}(r)$ in different samples are mostly overlapped, one can observe a slight enhancement on the second peak with decreasing cooling rate. In Fig. 4(b), all the peaks are enhanced in the slower cooled samples. And the sample prepared with sub-T_g annealing always has the highest peaks in both $g_{AlAl}(r)$ and $g_{AlSm}(r)$. In Fig. 4(c), $g_{SmSm}(r)$ shows the most noticeable change among different samples. When the cooling rate decreases, the first peak of $g_{SmSm}(r)$ decreases dramatically and becomes sharper, while the second peak at the range between 5.1 Å and 7.2 Å tends to split to two peaks. The sample prepared with sub-T_g annealing follows the same trends and shows the largest deviation from the fast quenched samples, suggesting it is effectively the "slowest" cooled glass among all the samples. Furthermore, a small side peak at r = 4.8 Å splitting from the first peak is only observed in two slowest samples: the sample quenched with10^9 K/s and the annealed sample, while the side peak in the annealed sample is stronger.

Based on the partial pair correlation functions, the structure factors $S(q)$ of MD models at T = 300 K are calculated and compared with the experimental measurement reported in Ref. [40] as shown in Fig. 4(d). Although there is a slight shift of peak positions at high-q, the main peaks from simulations and experiments agree well. Furthermore, the

prepeak at ~1.3 $Å^{-1}$, which is an intrinsic feature of Al-rich MGs [9,23], is also well captured by the simulations. As shown in the insert of Fig. 4(d), the sample prepared with sub-T_g annealing shows a much stronger prepeak than the continuously cooled samples. Since the prepeak at the low-q region generally reflects certain medium-range correlations in real space[41], lowering the effective cooling rate enhances the MRO in the system and brings the MRO closer to real MG.

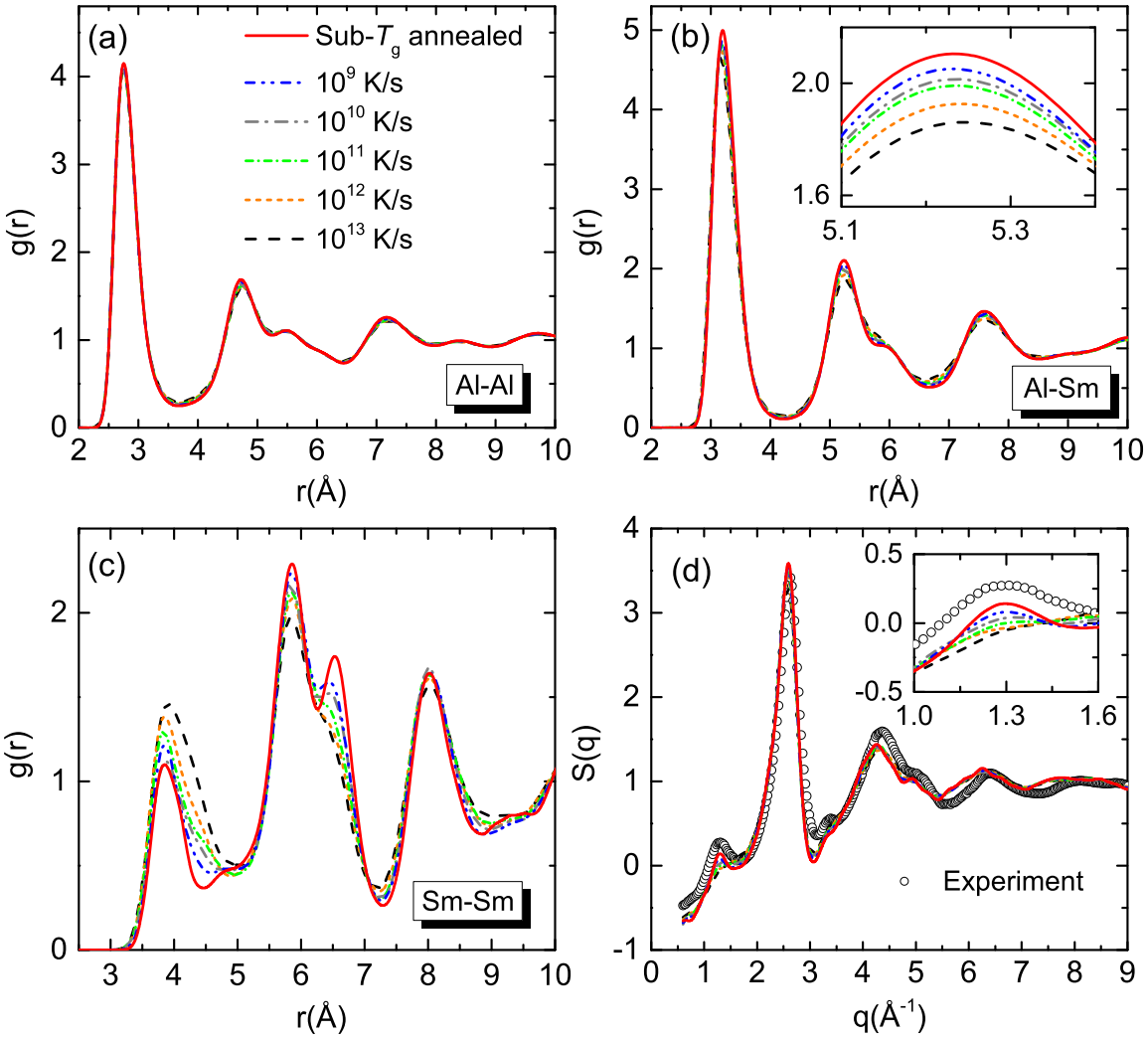

FIG. 4 (a)-(c) Partial pair correlation function of Al-Al, Al-Sm and Sm-Sm at 300 K for the simulated $Al_{90}Sm_{10}$ glass samples, respectively. The insert in (c) zooms in the second peak of Al-Sm partial pair correlation functions for clarity. (d) The total structure factor

of the MD models and experimental measurement at room temperature. The insert zooms in the pre-peak at low-q region. The experimental data (open circle) is taken from Ref. [40].

To understand topological packing in the glass models, we first characterize the local SRO in the system. Because of the large size disparity and mixing enthalpy between Al and Sm atoms, the overall structure feature is mostly determined by the solute Sm-centered ordering in this solute-lean system [26,42]. Here, we focus on studying how the Sm-centered "3661" clusters, which we identified in undercooled $Al_{90}Sm_{10}$ liquids [26], develop in glassy samples. The score distribution of alignment with the "3661" template for all the MD samples is shown in Fig. 5(a). The glassy structure displays better "3661" order when prepared with slower cooling rate, as the distribution function gradually shifts toward the lower values of the alignment score. The score distribution of the inherent structure at the beginning of the long annealing process is also included in Fig. 5(a), further showing the effect of sub-T_g annealing on enhancing the "3661" order. Here, for all the samples shown in Fig. 5(a), the deviation of non-"3661" clusters from the ideal template is continuous, leading to gradually increasing alignment scores. Thus, no separate peak characterizing non-"3661" Sm-centered clusters is observed. Since the glass sample should have much less distortion in the structural orders than that of liquid sample, we choose a strict cutoff value of 0.16, which is smaller than the one used for the liquid samples[26], to classify the "3661"-type clusters in glass. The fraction of "3661" clusters in all the MD samples is plotted as a function of cooling rate in Fig. 5(b). The sample obtained from the sub-T_g 650 K annealing contains more "3661" clusters than the other continuous cooled samples. The plot shows an approximately linear dependence between the fraction of "3661" clusters and the logarithm of the effective cooling rate,

which is quite similar to the behavior of the icosahedral SRO in the Cu-Zr system[33]. In Fig. 5(c), the population of "3661" cluster is compared with other AlSm cluster motifs, such as the Sm-centered clusters from observed β-Al_4Sm phase and α-$A_{l1}Sm_3$ phase. These two phases are both observed in the experiments[25], and the motifs of the Sm-centered clusters are found to be topologically different with 3661[26]. As other motifs only show vanishing populations, it indicates that "3661" motif is always the most dominating SRO in the $Al_{90}Sm_{10}$ undercooled liquid and glass samples, independent on the temperature, cooling rate used during quenching, or the cut-off value for the alignment scheme[26]. To understand the development of structure orders, we calculated the evolution of "3661" clusters in the inherent structures of samples during quenching. Here, we take the snapshots from the trajectory during $Al_{90}Sm_{10}$ cooling process (with cooling rate 10^{10} K/s), and instantaneously quench each snapshot to 0 K to obtain inherent structures. Then the "3661"-type Sm-centered clusters in the inherent structures are identified with the cluster alignment scheme. As shown in Fig. 5(d), upon decreasing the temperature, the population of "3661"-type cluster increases rapidly above T_g and nearly reaches a nearly constant value after passing the sub-T_g (650 K) region, suggesting that annealing at a sub-T_g temperature around 650 K is ideal for further development of the "3661" order. Considering the linear dependence of potential energy on the logarithm of the effective cooling rate as shown in Fig. 3, the increase of "3661" orders lowers the system energy and enhances the stability of the glass.

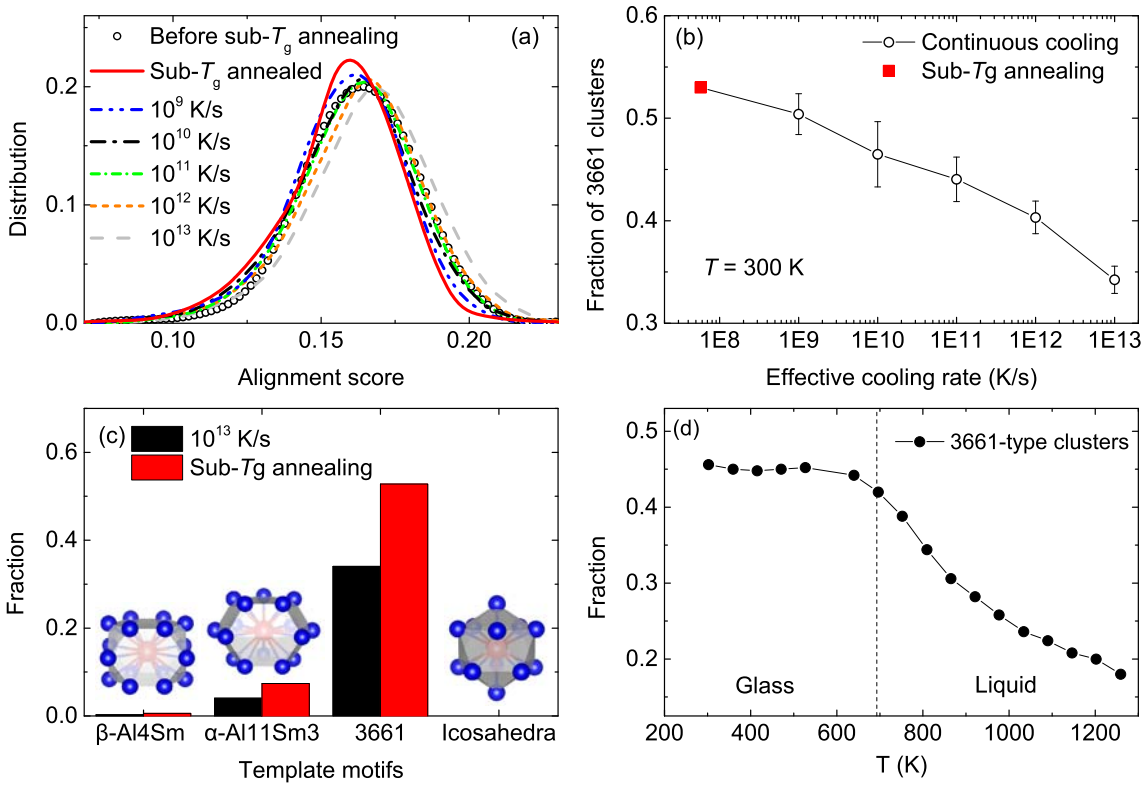

FIG. 5 (a) The distribution of the alignment score for Sm-centered clusters extracted from different MD samples. The lines show the samples at 300 K, while the open circle shows the inherent structure before sub-T_g annealing. (b) The fraction of "3661" clusters in each sample as a function of effective cooling rate. A cutoff alignment score of 0.16 was used to collect "3661"-type clusters. (c) The population of different cluster motifs in the samples using fastest cooling rate and sub-T_g annealing. The β-Al4Sm motif and α-Al11Sm3 motif are extracted from Al4Sm and Al11Sm3 phase, respectively. (d) The evolution of "3661"-type clusters in the inherent structures of the continuously cooled sample with cooling rate 10^{10} K/s. The dash line shows the glass transition temperature.

Next, we study how the structural order is extended to medium range by examining how these SRO clusters are arranged globally in the three-dimensional space[17]. Here, we introduce the radial distribution function of the center atoms in "3661" clusters G_c(r) to show the correlation among the "3661" clusters. G_c(r) is defined as $G_c(r) =$

$4\pi r^2 \rho_c g_c(r)$, where $g_c(r)$ is the pair correlation function calculated only for the center Sm atom in "3661" clusters and ρ_c is the number density of the "3661" centers in the sample. As shown in Fig. 6(a), while the other peaks show strong dependence on the cooling process, the first peak of G_c(r) largely overlaps for all the glass samples. The first peak is originated from interpenetrating connection of two neighboring "3661" clusters, i.e., the centers of the two clusters form a nearest-neighbor pair. An example of such interpenetration is given in the insert of Fig. 6(b). The overlapping of the first peak indicates that the interpenetrating connectivity is almost the same. In fact, for all the samples, about ~70% of the "3661" clusters do not have any interpenetrating neighbors, and most of the remaining "3661" clusters only have one neighbor, forming a "dimer"-like structure. It is interesting to note that even in the annealed sample, the "3661" clusters still only form dimers, instead of other superclusters with higher degrees. This is strikingly different from some strong glass formers such as $Cu_{64.5}Zr_{35.5}$, in which the icosahedral clusters form an extensive interpenetrating network that can percolate through the entire sample [34,43,44].

Since interpenetration of two clusters is characterized by the fact that a vertex of one cluster is the center of the other, we then check the possibility of each of the 16 vertices of a "3661" cluster being the center of a neighboring "3661" cluster. As shown in Fig. 6(c), the Vertex 17 in the insert of Fig. 6(c) has the highest possibility [this way of interpenetration is shown in the insert of Fig. 6(b)], while the other 15 vertices can also be interpenetrated. Thus, there can be multiple ways of interpenetration for two neighboring "3661" clusters, which give rise to the ripples in the interpenetration curve in Fig. 6(b). In the metastable devitrification products, only interpenetrated dimers

illustrated in Fig. 6(b) are present[27,28], suggesting this way of interpenetration is energetically the most favorable.

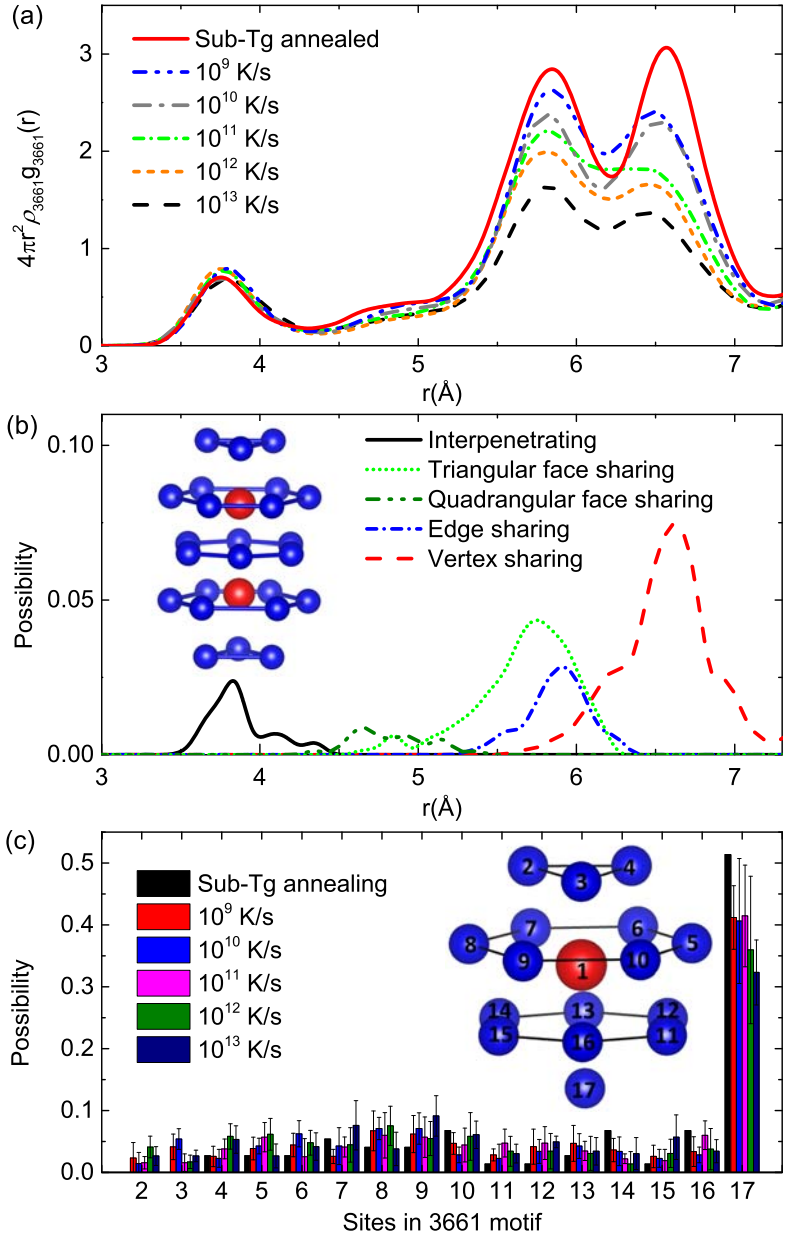

FIG. 6 (a) The radial distribution function calculated using only the centers of "3661" clusters in the glass models prepared with various cooling process. (b) The distributions of the distance between two "3661" cluster centers adopting each type of connection in the model prepared by sub-T_g annealing. The insert shows one possible way of interpenetration between two "3661" clusters. The blue balls indicate Al atoms, while the

red balls indicate Sm atoms. (c) The possibility of each of the vertices of a "3661" cluster being the center of a neighboring "3661" cluster. The corresponding vertex index is shown in the inserted "3661" cluster.

While the first peak of $G_c(r)$ is very similar for the samples with different cooling process, the intensities of other peaks are dramatically enhanced with decreasing cooling rates. Furthermore, the splitting of the peak in the distance range between 5.1 Å and 7.2 Å is much stronger in $G_c(r)$ than that in the corresponding Sm-Sm pair-correlation $g_{SmSm}(r)$ in all the samples. Thus, the correlation among Sm-centered "3661" clusters makes a significant contribution to $g_{SmSm}(r)$ at distances beyond 4.5 Å. By analyzing the network between "3661" clusters in the sub-T_g annealed sample, the peaks of $G_c(r)$ can be assigned to the different connecting types as shown in Fig. 6 (b). It can be seen that the peaks centered at 3.8 Å and 6.6 Å correspond to interpenetrating and vertex-sharing connection types of "3661" clusters, respectively. The peak at 5.8 Å is attributed to collective contributions from edge sharing and triangular face sharing. The broad peak between 4.5 Å and 5.0 Å is mainly due to both triangular and quadrangular face sharing. These results demonstrate that while interpenetrating connections remain similar, the sub-T_g annealing enhances MRO by promoting edge, face, and vertex sharing of SRO clusters.

In summary, we performed MD simulations using sub-T_g annealing and continuous cooling techniques to generate atomistic models for $Al_{90}Sm_{10}$ MG. We showed that the structure factor of the sub-T_g annealed sample is closer to the experimental result, indicating a closer atomic structure to the experimental MG. Using the cluster alignment method, we identified the "3661" cluster as the characteristic SRO of the system. Both SRO and MRO, which is defined by the global arrangement of SRO

clusters, significantly enhance as the cooling rate reduces. On the other hand, unlike strong glass formers, interpenetrating SRO clusters do not form an extensive interpenetrating network even for the sub-T_g annealed sample, which could be responsible for the marginal glass-formability of the $Al_{90}Sm_{10}$ system.

Acknowledgements

Work at Ames Laboratory was supported by the US Department of Energy, Basic Energy Sciences, Division of Materials Science and Engineering, under Contract No. DE-AC02-07CH11358, including a grant of computer time at the National Energy Research Supercomputing Center (NERSC) in Berkeley, CA. Y.S. acknowledges the support from China Scholarship Council (File No. 201406340015). Z.J.D. acknowledges support from the National Natural Science Foundation of China (No. 11274288 and No. 11574289) and the National Basic Research Program of China (No. 2012CB933702).

Reference

[1] W. Klement, R.H. Willens, and P. Duwez, Nature **187**, 869 (1960).

[2] P. Chaudhari and D. Turnbull, Science **199**, 11 (1978).

[3] H.S. Chen, Rep. Prog. Phys. **43**, 353 (1980).

[4] A.L. Greer, Science **267**, 1947 (1995).

[5] W.H. Wang, C. Dong, and C.H. Shek, Mater. Sci. Eng. R **44**, 45 (2004).

[6] A. Inoue, Acta Mater. **48**, 279 (2000).

[7] J. Schroers, Adv. Mater. **22**, 1566 (2010).

[8] M. Chen, NPG Asia Mater. **3**, 82 (2011).

[9] Y.Q. Cheng and E. Ma, Prog. Mater. Sci. **56**, 379 (2011).

[10] K.F. Kelton, G.W. Lee, A.K. Gangopadhyay, R.W. Hyers, T.J. Rathz, J.R. Rogers,

M.B. Robinson, and D.S. Robinson, Phys. Rev. Lett. **90**, 195504 (2003).

[11] T. Schenk, D. Holland-Moritz, V. Simonet, R. Bellissent, and D.M. Herlach, Phys. Rev. Lett. **89**, 75507 (2002).

[12] A. Hirata, P. Guan, T. Fujita, Y. Hirotsu, A. Inoue, A.R. Yavari, T. Sakurai, and M. Chen, Nat. Mater. **10**, 28 (2011).

[13] J.D. Bernal and J. Mason, Nature **188**, 910 (1960).

[14] D.B. Miracle, Nat. Mater. **3**, 697 (2004).

[15] P.H. Gaskell, Nature **276**, 484 (1978).

[16] A. Haji-Akbari, M. Engel, A.S. Keys, X. Zheng, R.G. Petschek, P. Palffy-Muhoray, and S.C. Glotzer, Nature **462**, 773 (2009).

[17] H.W. Sheng, W.K. Luo, F.M. Alamgir, J.M. Bai, and E. Ma, Nature **439**, 419 (2006).

[18] X.J. Liu, Y. Xu, X. Hui, Z.P. Lu, F. Li, G.L. Chen, J. Lu, and C.T. Liu, Phys. Rev. Lett. **105**, (2010).

[19] P.F. Guan, T. Fujita, A. Hirata, Y.H. Liu, and M.W. Chen, Phys. Rev. Lett. **108**, 175501 (2012).

[20] F.H. Stillinger and T.A. Weber, Science **225**, 983 (1984).

[21] A. Inoue, Prog. Mater. Sci. **43**, 365 (1998).

[22] A. Inoue, K. Ohtera, Z. Tao, and T. Masumoto, Jpn. J. Appl. Phys. **27**, L1583 (1988).

[23] Y.E. Kalay, C. Yeager, L.S. Chumbley, M.J. Kramer, and I.E. Anderson, J. Non. Cryst. Solids **356**, 1416 (2010).

[24] N. Wang, Y.E. Kalay, and R. Trivedi, Acta Mater. **59**, 6604 (2011).

[25] S.H. Zhou and R.E. Napolitano, Metall. Mater. Trans. A **38**, 1145 (2007).

[26] Y. Sun, F. Zhang, Z. Ye, Y. Zhang, X. Fang, Z. Ding, C.-Z. Wang, M.I. Mendelev, R.T.

Ott, M.J. Kramer, and K.-M. Ho, Sci. Rep. **6**, 23734 (2016).

[27] Z. Ye, F. Zhang, Y. Sun, M.C. Nguyen, M.I. Mendelev, R.T. Ott, E.S. Park, M. Besser, M.J. Kramer, Z.-J. Ding, C.-Z. Wang, and K.-M. Ho, "Unconventional phase selection in high-driven systems: A complex metastable structure prevails over simple stable phases", Phys. Rev. Lett. (submitted), preprint arXiv:1502.00023 (2015).

[28] Z. Ye, F. Zhang, Y. Sun, M.I. Mendelev, R.T. Ott, E. Park, M.F. Besser, M.J. Kramer, Z. Ding, C.-Z. Wang, and K.-M. Ho Appl. Phys. Lett. **106**, 101903 (2015).

[29] A.R. Leach, *Molecular Modelling: Principles and Applications* (Prentice Hall, 2001).

[30] P.G. Debenedetti and F.H. Stillinger, Nature **410**, 259 (2001).

[31] M.J. Kramer, H. Mecco, K.W. Dennis, E. Vargonova, R.W. McCallum, and R.E. Napolitano, J. Non. Cryst. Solids **353**, 3633 (2007).

[32] M.P. Allen and D.J. Tildesley, *Computational Simulation of Liquids* (Clarendon Press, 1991).

[33] F. Zhang, M.I. Mendelev, Y. Zhang, C.-Z. Wang, M.J. Kramer, and K.-M. Ho, Appl. Phys. Lett. **104**, 061905 (2014).

[34] Y. Zhang, F. Zhang, C.-Z. Wang, M.I. Mendelev, M.J. Kramer, and K.-M. Ho, Phys. Rev. B **91**, 064105 (2015).

[35] X.W. Fang, C.-Z. Wang, Y.X. Yao, Z.J. Ding, and K.-M. Ho, Phys. Rev. B **82**, 184204 (2010).

[36] M.I. Mendelev, F. Zhang, Z. Ye, Y. Sun, M.C. Nguyen, S.R. Wilson, C.-Z. Wang, and K.-M. Ho, Model. Simul. Mater. Sci. Eng. **23**, 45013 (2015).

[37] T.E. Faber and J.M. Ziman, Philos. Mag. **11**, 153 (1965).

[38] D. Waasmaier and A. Kirfel, Acta Crystallogr. **51**, 416 (1995).

[39] Y.Q. Cheng, A.J. Cao, and E. Ma, Acta Mater. **57**, 3253 (2009).

[40] Y.E. Kalay, L.S. Chumbley, M.J. Kramer, and I.E. Anderson, Intermetallics **18**, 1676 (2010).

[41] F. Zhang, Y. Sun, Z. Ye, Y. Zhang, C.-Z. Wang, M.I. Mendelev, R.T. Ott, M.J. Kramer, Z.-J. Ding, and K.-M. Ho, J. Phys. Condens. Matter **27**, 205701 (2015).

[42] D.B. Miracle and O.N. Senkov, J. Non. Cryst. Solids **319**, 174 (2003).

[43] R. Soklaski, Z. Nussinov, Z. Markow, K.F. Kelton, and L. Yang, Phys. Rev. B **87**, 184203 (2013).

[44] J. Ding, Y.-Q. Cheng, and E. Ma, Acta Mater. **69**, 343 (2014).

Figure Captions

FIG. 1 (a) The side view of "3661" motif; (b) the top view of "3661" motif. The red atom indicates the center Sm, while the blue atoms indicate the first-shell atoms.

FIG. 2 The validation of AlSm Finnis-Sinclair potential. (a)-(d) The comparison of total and partial pair distribution functions of $Al_{90}Sm_{10}$ undercooled liquid at 800 K obtained by previous *ab initial* MD[26] and current classical MD with the Finnis-Sinclair potential. (e) The comparison of alignment score with "3661" template for Sm atoms in $Al_{90}Sm_{10}$ liquid at 800 K obtained by *ab initial* MD and classical MD.

FIG. 3 Potential energy at 300K as a function of cooling rate. The blue line is the least-square fitting to a logarithmic dependence for all continuous cooled samples. The red arrow points an effective continuous cooling rate of 5.7×10^7 K/s achieved by sub-T_g annealing.

FIG. 4 (a)-(c) Partial pair correlation function of Al-Al, Al-Sm and Sm-Sm at 300 K for the simulated $Al_{90}Sm_{10}$ glass samples, respectively. The insert in (c) zooms in the second peak of Al-Sm partial pair correlation functions for clarity. (d) The total structure factor of the MD models and experimental measurement at room temperature. The insert zooms in the pre-peak at low-q region. The experimental data (open circle) is taken from Ref. [40].

FIG. 5 (a) The distribution of the alignment score for Sm-centered clusters extracted from different MD samples. The lines show the samples at 300 K, while the open circle shows the inherent structure before sub-T_g annealing. (b) The fraction of "3661" clusters in each sample as a function of effective cooling rate. A cutoff alignment score of 0.16 was used to collect "3661"-type clusters. (c) The population of different cluster motifs in the samples using fastest cooling rate and sub-T_g annealing. The β-Al4Sm motif and α-

Al11Sm3 motif are extracted from Al4Sm and Al11Sm3 phase, respectively. (d) The evolution of "3661"-type clusters in the inherent structures of the continuously cooled sample with cooling rate 10^{10} K/s. The dash line shows the glass transition temperature.

FIG. 6 (a) The radial distribution function calculated using only the centers of "3661" clusters in the glass models prepared with various cooling process. (b) The distributions of the distance between two "3661" cluster centers adopting each type of connection in the model prepared by sub-T_g annealing. The insert shows one possible way of interpenetration between two "3661" clusters. The blue balls indicate Al atoms, while the red balls indicate Sm atoms. (c) The possibility of each of the vertices of a "3661" cluster being the center of a neighboring "3661" cluster. The corresponding vertex index is shown in the inserted "3661" cluster.

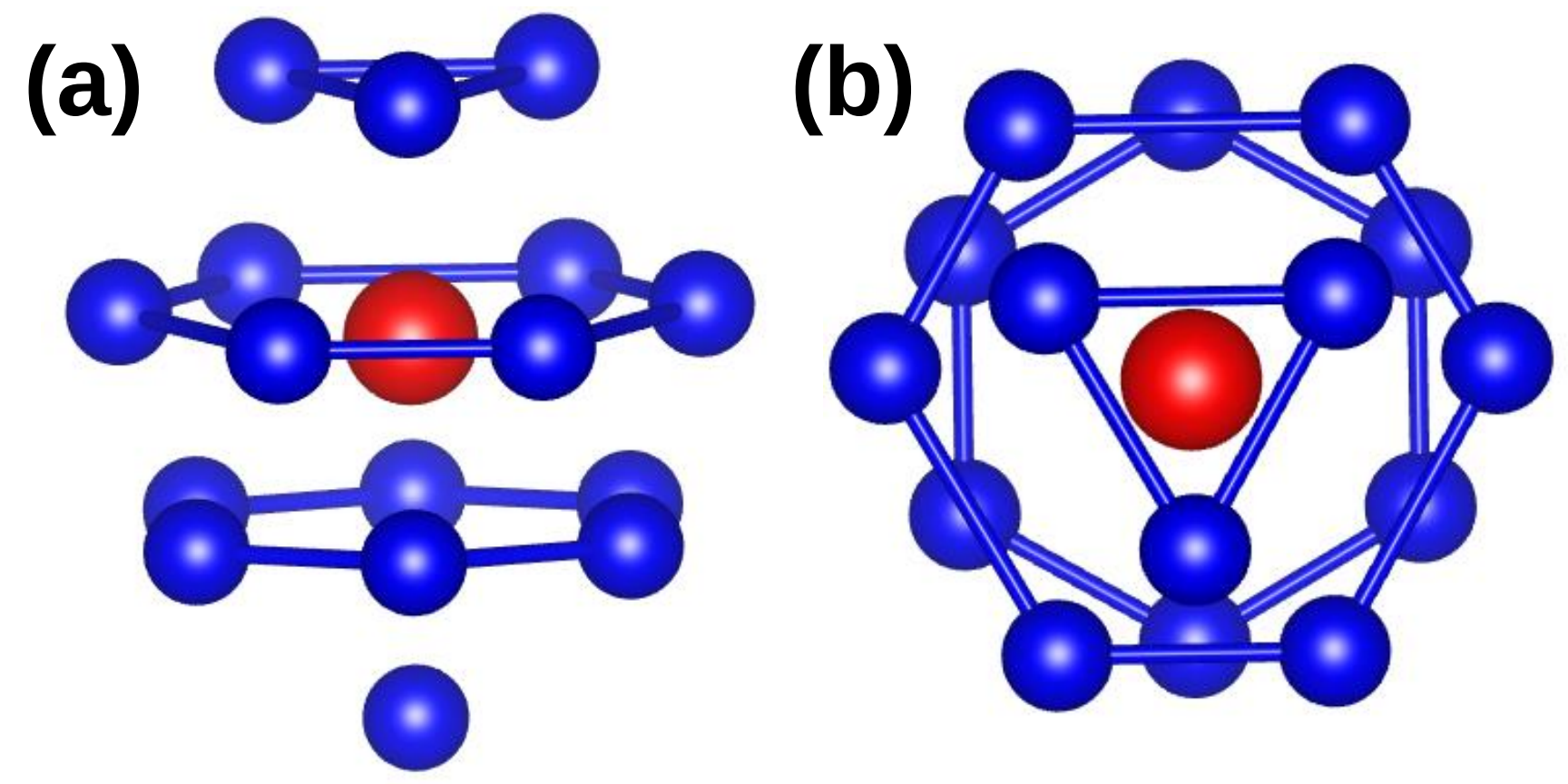
(a)
(b)

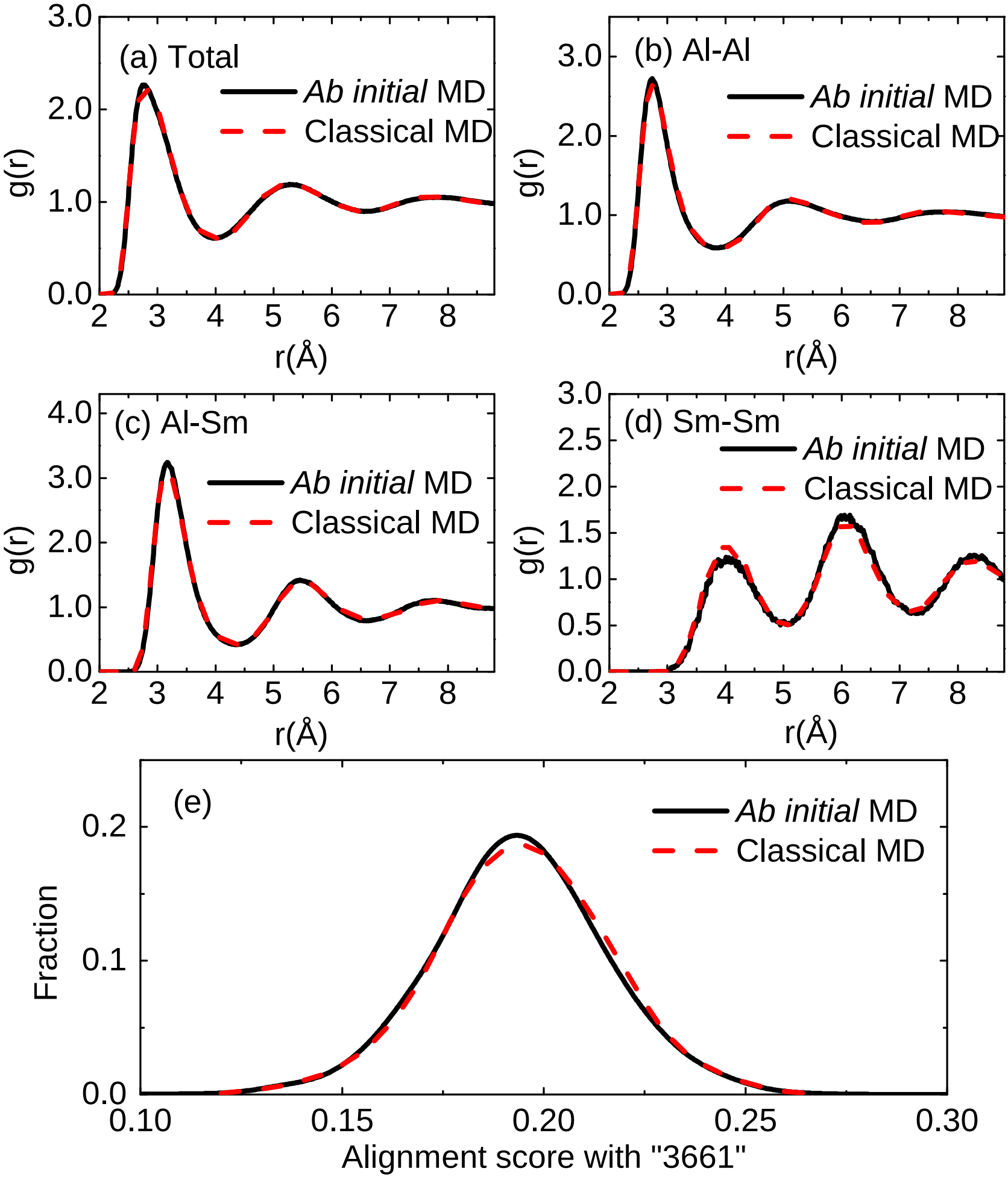
(a) Total
(b) Al-Al
(c) Al-Sm
(d) Sm-Sm
(e)
Ab initial MD
Classical MD
g(r)
r(Å)
Fraction
Alignment score with "3661"

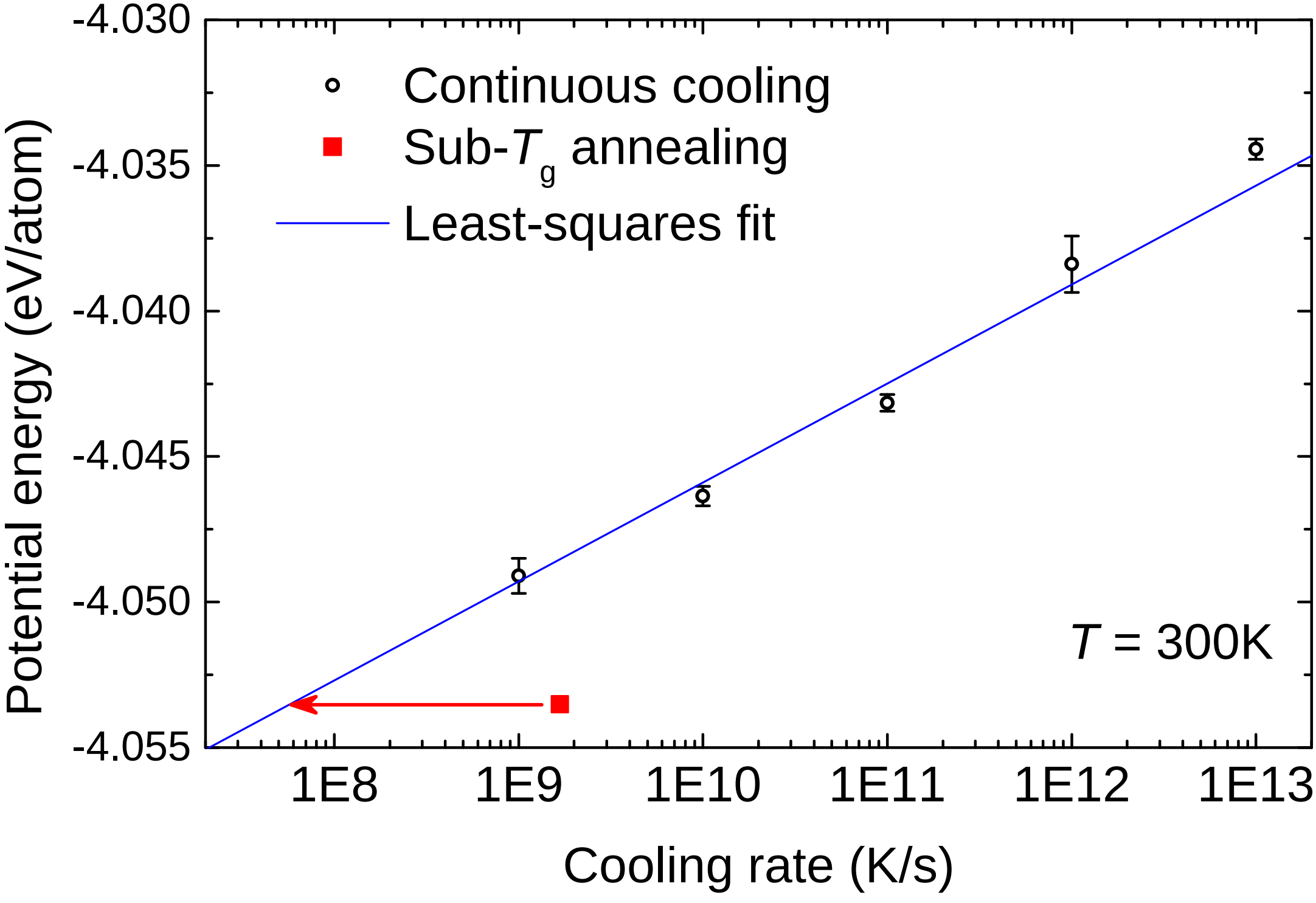
Continuous cooling
Sub-T_g annealing
Least-squares fit
T = 300K
Potential energy (eV/atom)
-4.030
-4.035
-4.040
-4.045
-4.050
-4.055
1E8
1E9
1E10
1E11
1E12
1E13
Cooling rate (K/s)

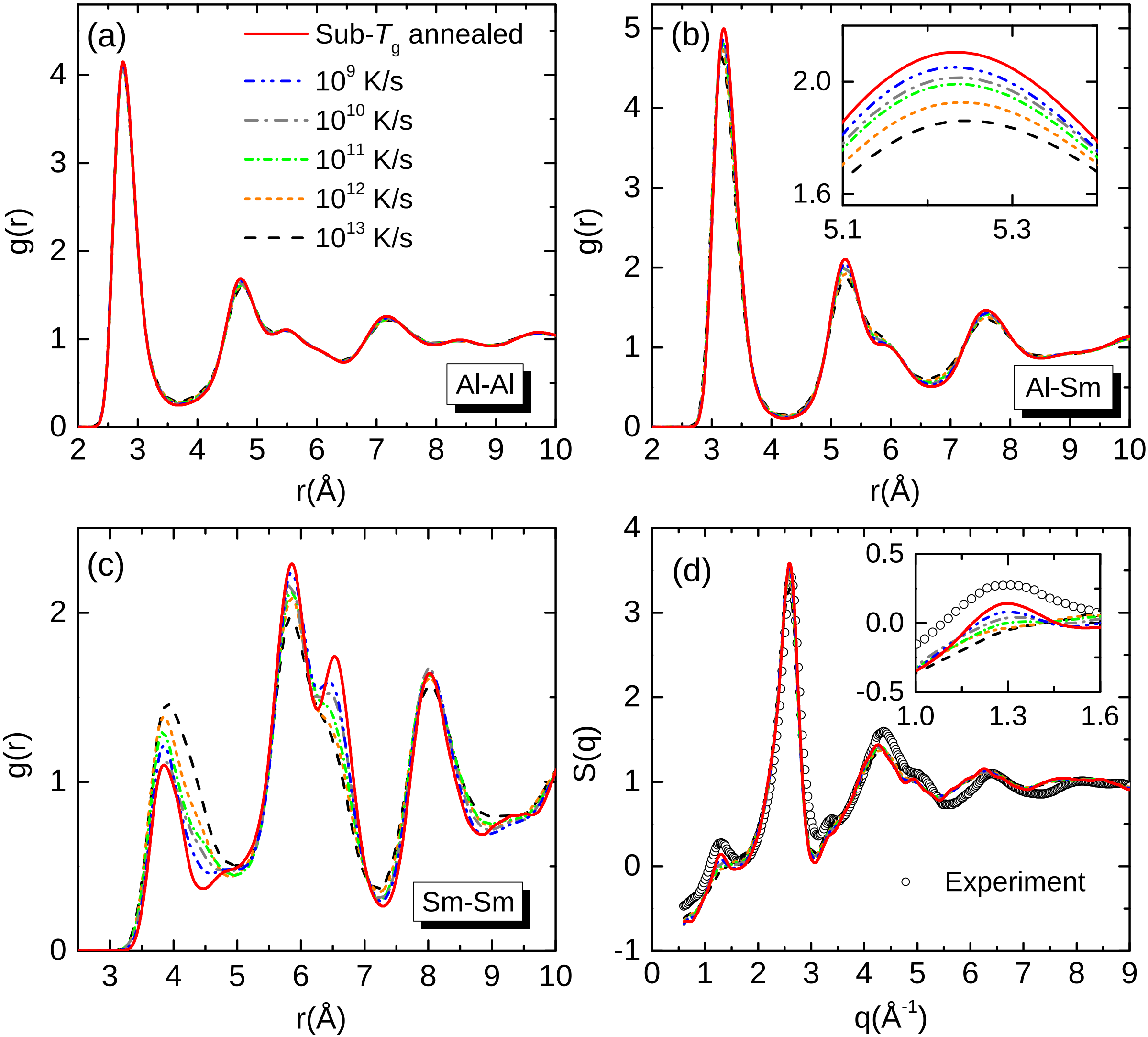
(a)
Sub-T_g annealed
10^9 K/s
10^{10} K/s
10^{11} K/s
10^{12} K/s
10^{13} K/s
Al-Al
g(r)
r(Å)
(b)
Al-Sm
g(r)
r(Å)
(c)
Sm-Sm
g(r)
r(Å)
(d)
Experiment
S(q)
q(Å^{-1})

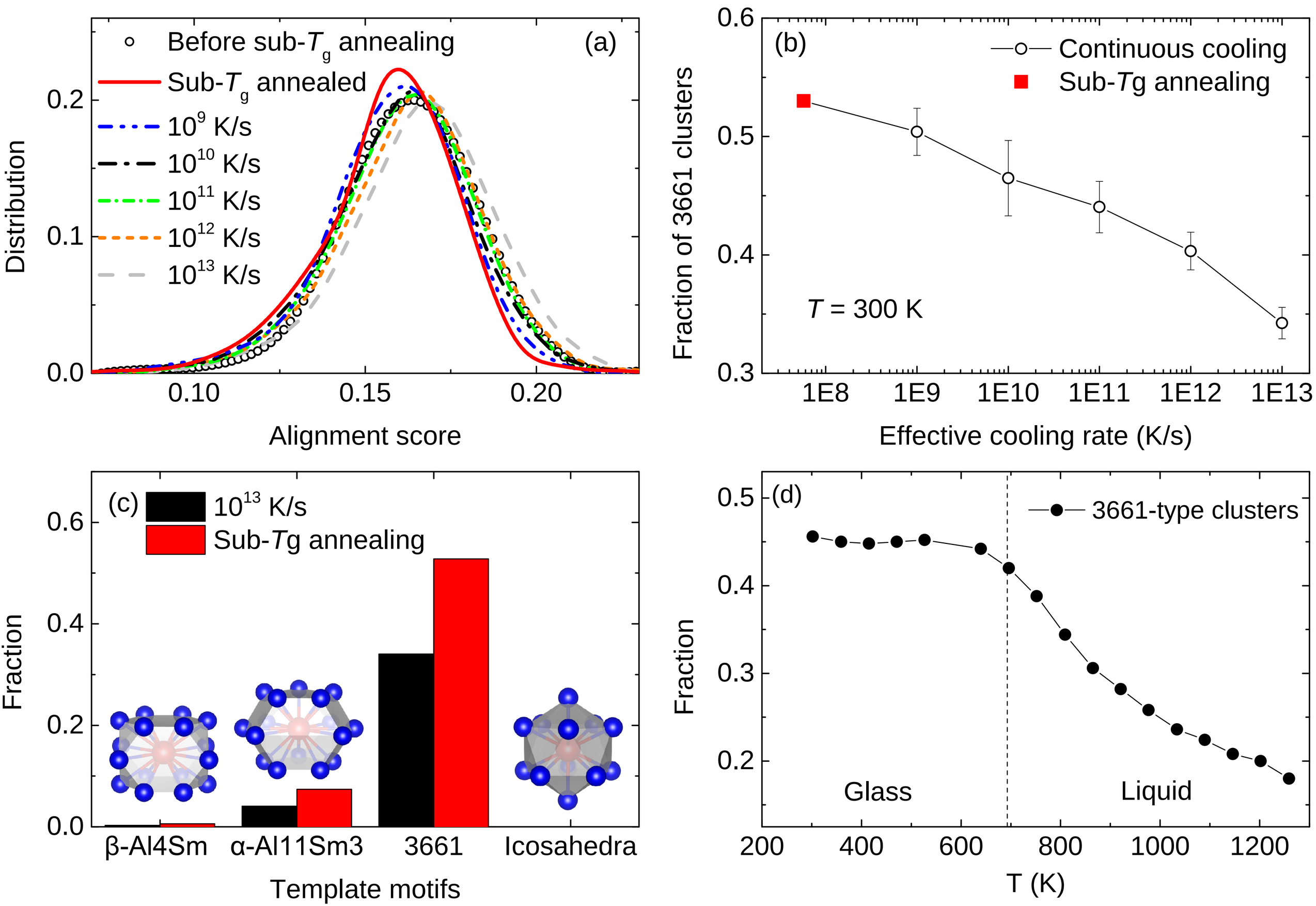
(a)
Before sub-T_g annealing
Sub-T_g annealed
10^9 K/s
10^{10} K/s
10^{11} K/s
10^{12} K/s
10^{13} K/s
Distribution
Alignment score
(b)
Continuous cooling
Sub-Tg annealing
T = 300 K
Fraction of 3661 clusters
Effective cooling rate (K/s)
(c)
10^{13} K/s
Sub-Tg annealing
Fraction
β-Al4Sm
α-Al11Sm3
3661
Icosahedra
Template motifs
(d)
3661-type clusters
Glass
Liquid
Fraction
T (K)

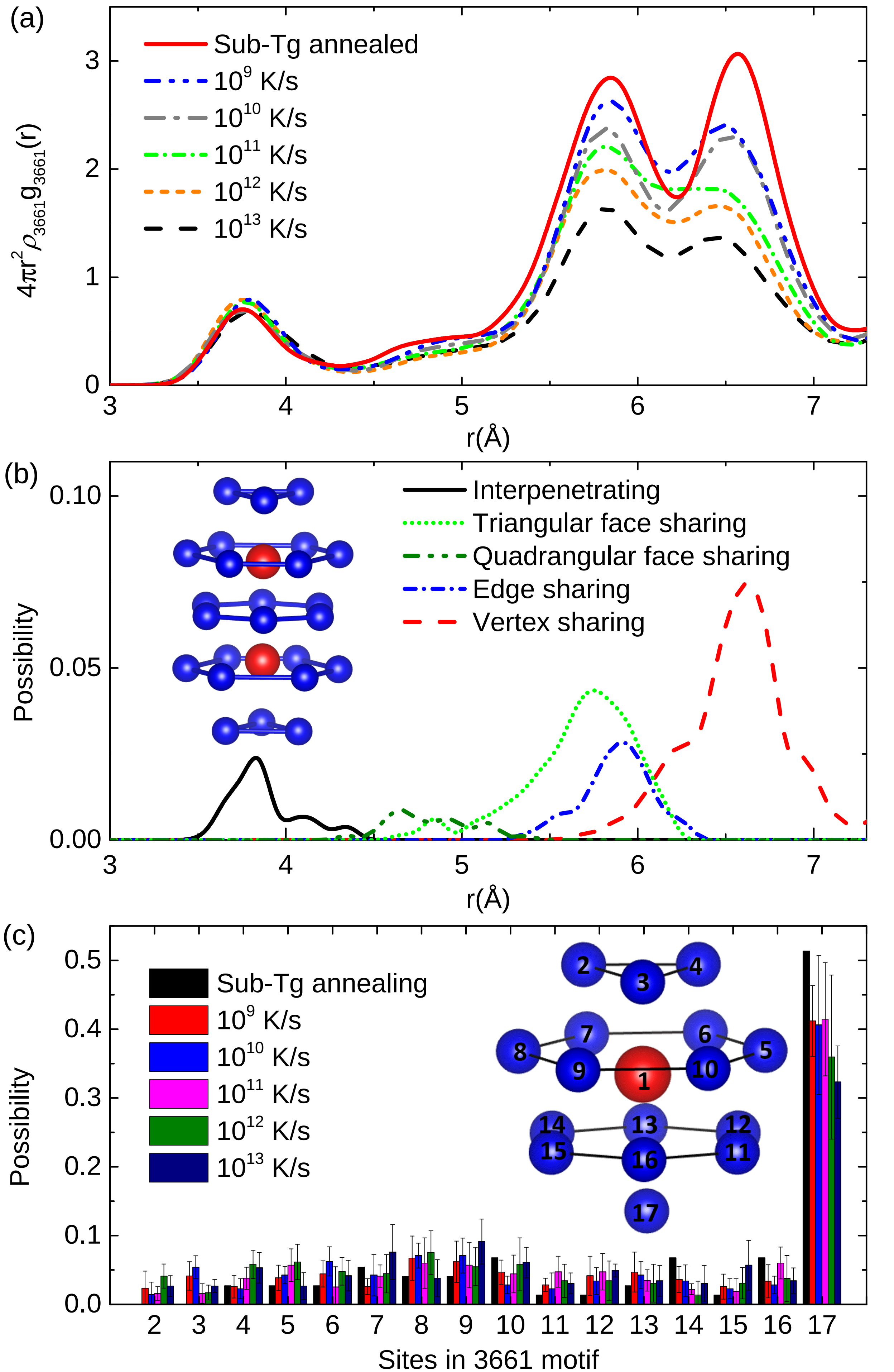
(a)
Sub-Tg annealed
10^9 K/s
10^10 K/s
10^11 K/s
10^12 K/s
10^13 K/s
4πr²ρ3661g3661(r)
r(Å)
(b)
Interpenetrating
Triangular face sharing
Quadrangular face sharing
Edge sharing
Vertex sharing
Possibility
r(Å)
(c)
Sub-Tg annealing
10^9 K/s
10^10 K/s
10^11 K/s
10^12 K/s
10^13 K/s
Possibility
Sites in 3661 motif